

See discussions, stats, and author profiles for this publication at: <https://www.researchgate.net/publication/261271824>

Tetrabromoterephthalic Acid in Designing Co-crystals and Salts: Modification of Optical Properties and Schottky Barrier Effect

ARTICLE in CRYSTAL GROWTH & DESIGN · NOVEMBER 2013

Impact Factor: 4.89 · DOI: 10.1021/cg4014009

CITATIONS

5

READS

29

9 AUTHORS, INCLUDING:



Rajat Saha

Jadavpur University

58 PUBLICATIONS 306 CITATIONS

SEE PROFILE



Susobhan Biswas

Jadavpur University

34 PUBLICATIONS 160 CITATIONS

SEE PROFILE



Michel Fleck

University of Vienna

141 PUBLICATIONS 1,186 CITATIONS

SEE PROFILE



Sanjay Kumar

Jadavpur University

44 PUBLICATIONS 322 CITATIONS

SEE PROFILE

Tetrabromoterephthalic Acid in Designing Co-crystals and Salts: Modification of Optical Properties and Schottky Barrier Effect

Sanjoy Kumar Dey,^{†,‡} Rajat Saha,^{*,†} Susobhan Biswas,[†] Animesh Layek,[†] Somnath Middya,[†] Ian M. Steele,[§] Michel Fleck,^{||} Partha Pratim Ray,[†] and Sanjay Kumar^{*,†}

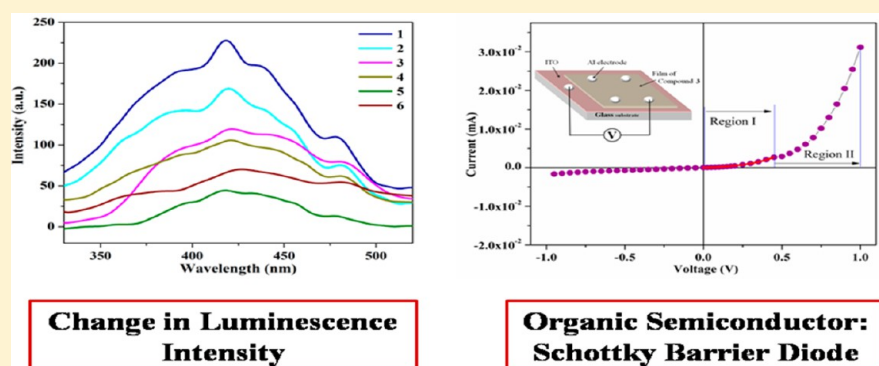
[†]Department of Physics, Jadavpur University, Jadavpur, Kolkata 700 032, India

[‡]Department of Physics, NITMAS, 24 paragana(S), West Bengal 743368, India

[§]Department of the Geophysical Sciences, The University of Chicago, Chicago, Illinois 60637, United States

^{||}Institute of Mineralogy and Crystallography Geozentrum, University of Vienna, Althanstrasse 14 A 1090 Vienna, Austria

Supporting Information



ABSTRACT: Herein, tetrabromoterephthalic acid (TBTA) is used as the potential co-crystal former with various organic base molecules containing free nitrogen atoms. The crystal structure of TBTA (compound 1) has been determined from powder X-ray diffraction (PXRD) data. In a systematic way, we have synthesized hydrated-TBTA (compound 2), two salts of TBTA [TBTA²⁻-4,4'-bipy²⁺ (compound 3), 4,4'-bipy = 4,4'-bipyridine, and TBTA²⁻-(3-AP⁺)₂ (compound 4), 3-AP = 3-aminopyridine] and two co-crystals of TBTA [TBTA-DPTZ (compound 5), DPTZ = 3,6-di(pyridyl-2-yl)-1,2,4,5-tetrazine, and TBTA-(3-IP)₂ (compound 6), 3-IP = 3-iodopyridine]. All of the compounds were characterized by structural, spectral, and thermal studies. Supramolecular structural analysis reveals that 1 forms a 2D supramolecular sheet structure by means of O-H...Br hydrogen bonding interactions and hydrated-2 forms a 3D supramolecular structure through water mediated hydrogen bonding interactions and $\pi\cdots$ interactions. The O-H...N/O⁻...H-N⁺ hydrogen bonding interactions between acid and base molecules give rise to 1D supramolecular chain structure in 3 and supramolecular trimers in 4, 5, and 6. Because of presence of charge assisted O⁻...H-N⁺ hydrogen bonds between acid-base molecules, 3 and 4 form hydrogen bonds with solvent water molecules, and also both 3 and 4 form 3D supramolecular structures using both hydrogen bonding and $\pi\cdots$ interactions. In co-crystal 5, solvent water molecules participate in crystallization in contrast to 6, and it has been observed that 5 forms 3D supramolecular structure, while 6 forms 2D supramolecular structure using both hydrogen bonding and $\pi\cdots$ interactions. An investigation of intermolecular closed contacts has been carried out by Hirshfeld surface analysis, and associated 2D fingerprint plots reveal the similarities and differences of TBTA molecules in these six crystal structures. Photoluminescence spectra of all the compounds have been studied, and they reveal that with change of polarity around TBTA luminescent intensity of the compounds has been modified. *I*-*V* measurement indicates that 3 shows semiconducting behavior, and the ITO/3/Al sandwich structure acts as a Schottky barrier diode. The device exhibits an excellent rectification ratio (19 at ± 1 V) with an ideality factor of 2.96. The semiconducting behavior of 3 is attributed to the formation charge assisted hydrogen bonding interactions between acid and base molecules.

INTRODUCTION

The primary goal of crystal engineering is to realize the intermolecular interactions in the context of crystal packing toward the design and synthesis of novel functional materials.¹ There are several types of weak intermolecular interactions, namely, hydrogen bonding, $\pi\cdots$ interactions, etc.; they intervene in the crystal packing during synthesis.² Deliberate research is in

progress to understand those weak interactions and to control them to synthesize designer crystals with predefined functional properties.³

Received: September 20, 2013

Revised: November 14, 2013

Published: November 26, 2013

The supramolecular assembly of two or more molecular components in the solid state, in the presence or absence of solvent molecules, is called a co-crystal. In the field of co-crystals, carboxylic acids have attracted much attention as excellent co-crystallizing agents because they take part in supramolecular hydrogen bonding interactions with other organic base molecules like pyridines. Numerous examples of binary acid–base co-crystals of bicarboxylic acids have been reported during the last decades, and such assembly has been driven through noncovalent interactions, mainly through hydrogen bonding interactions.⁴ It has been found that the formation of the O–H⋯N type of *heterosynthon* takes place between the carboxylic acids and the base molecules leading to co-crystallization.⁵ It has been observed that in several cases salt formation takes place by proton transfer from acid molecules to base molecules generating an ion pair and the ion pair gets stability through charge assisted O[−]⋯H–N⁺ hydrogen bonding interactions.⁶ It is worth mentioning that such carboxylic acids have a tendency to form hydrogen bonded eight membered {⋯H–O–C=O}₂ *homosynthon* type motifs.⁷

Since within the co-crystals and salts organic molecules interact through noncovalent interactions, it is expected that rational research will help to analyze “how an organic molecule having a specific functional group participates in supramolecular assembly with other organic molecules”.⁸ Thus, the study of co-crystals and salts will be more fruitful to understand those weak noncovalent forces that govern the formation of solid state structures.⁹ It is well-known that the physical and chemical properties of organic solids depend on molecular packing within the crystal structure and the supramolecular interactions within them; thus a recent trend in crystal engineering is the modification of functional properties of organic compounds through co-crystallization as well as development of novel functional properties.¹⁰ William Jones and his co-workers have tuned the photoluminescence properties of stilbene-type molecules through co-crystallization.¹¹ Christer B. Aakeröy and his co-workers have modified the aqueous solubility and melting behavior of hexamethylenebisacetamide, an anticancer drug.¹² The enhancement of electrical conductivity of organic materials through salt formation is a prime issue in the field of semiconductors. It has been reported that organic materials having extended π -conjugated electrons and charge assisted hydrogen bonds can exhibit semiconducting behavior.^{13–15} Kapadia and his co-workers have shown the semiconducting behavior of multicomponent salts of tetraphenylethylenetetracarboxylic acid and bipyridines via charge assisted hydrogen bonding interactions.¹³

Here, we have systematically used tetrabromoterephthalic acid (TBTA) to synthesize multicomponent co-crystals and salts and successfully established their relevant functional properties. Because of presence of an aromatic ring, four bromides, and two carboxylic acid groups, TBTA can participate in hydrogen bonding and π ⋯ interactions, and thus we have used TBTA to synthesize multicomponent co-crystals with other organic molecules through noncovalent interactions. Our target is to establish TBTA as an excellent co-crystal former and to find out how it interacts with other organic base molecules in a noncovalent way toward the design of new functional materials. In this background, we have primarily solved the crystal structure of TBTA (compound 1) from PXRD data and described its overall supramolecular structure. Then, we have attempted to synthesize multicomponent co-crystals of TBTA with different organic base molecules like (i) 1,2,4-triazole, (ii) 4,4′-bipyridine

(4,4′-bipy), (iii) 3-aminopyridine (3-AP), (iv) 3,6-di(pyridin-2-yl)-1,2,4,5-tetrazine (DPTZ), and (v) 3-iodopyridine (3-IP), but as a matter of fact, our efforts have given rise to the formation of hydrated-TBTA (compound 2), salt TBTA^{2−}–4,4′-bipy²⁺ (compound 3), salt TBTA^{2−}–(3-AP⁺)₂ (compound 4), co-crystal TBTA–DPTZ (compound 5), and co-crystal TBTA–(3-IP)₂ (compound 6). Structural characterization of 3 has been carried out using PXRD data, while all other compounds (2, 4, 5, and 6) were characterized using single crystal X-ray diffraction (SC-XRD) data. The supramolecular structures of all the compounds have been described in detail. An investigation of intermolecular closed contacts has been carried out via Hirshfeld surface analysis, and associated 2D fingerprint plots are utilized to analyze the similarities and differences of supramolecular interactions experienced by TBTA in all the crystal structures. Thermal analyses of all the compounds have been performed. Photoluminescence spectra of all the compounds have been studied and significant differences in their photoluminescence spectra have been observed. The physicochemical causes behind the genesis of such differences have been elucidated. In salt 3, acid and base molecules are connected by charge assisted hydrogen bonds to form 1D supramolecular chain, and thus we have investigated the electrical transport properties of 3. Interestingly, the ITO/3/Al sandwich structure displays “Schottky diode” behavior, and the relevant parameters such as ideality factor, barrier height, and series resistance of the Schottky diode have been evaluated from the current–voltage (*I*–*V*) characteristics.

■ EXPERIMENTAL SECTION

Materials and Methods. All the reagents, TBTA, 1,2,4-triazole, 4,4′-bipyridine, 3-iodopyridine, 3-aminopyridine, 3,6-di(pyridin-2-yl)-1,2,4,5-tetrazine, and all the solvents, were purchased from commercial sources and used without further purification. Elemental analyses (C, H, N analysis) were carried out using a PerkinElmer 240C elemental analyzer. IR studies were done on a Nicolet Impact 410 spectrometer between 400 and 4000 cm^{−1} using the KBr pellet method. Solid state UV–vis spectra were recorded in Varian Cary 5000 UV–vis–NIR absorption spectrophotometer at room temperature. Thermal analyses were performed on a TGA instruments TGA-Q500 thermogravimetric analyzer. The compounds were heated over the temperature range of 25–500 °C at a constant heating rate of 10 °C/min with a stream of N₂ gas throughout the experiment at 40 mL/min. Photoluminescence spectra were collected on a Shimadzu RF-5301PC spectrofluorometer.

Synthesis of Hydrated TBTA, 2 {(C₈H₄Br₄O₄)^{2−}·2(H₂O)}. TBTA (0.6 mmol, 0.289 g) was added to 10 mL of ethanol, and the solution was stirred for 15 min. 1,2,4-Triazole (0.4 mmol) was added to 10 mL of methanol, and the solution was stirred for 15 min. Then both solutions were mixed and stirred for another 10 min. The colorless solution was kept in open air at room temperature for slow evaporation. After 2 days, colorless block shaped crystals suitable for X-ray diffraction were obtained. Yield: 30%. IR: 3340(b), 2925(w), 2850(w), 1728(s), 1644(br), 1514(s), 1482(s), 1445(w), 1408(w), 1305(w), 1287(w), 1235(w), 1130(w), 1063(w), 817(w), 698(w), 571(w), 537(w), 524(w). Anal Calcd for 2: C 18.60% (18.54% theor); H 1.12% (1.16% theor).

Synthesis of Salt 3 {(C₈Br₄O₄)^{2−}·(C₁₀H₁₀N₂)²⁺·2(H₂O)}. TBTA (0.5 mmol, 0.241 g) was dissolved in 10 mL of ethanol–water (1:1, v/v) mixture. The solution was stirred for 30 min. 4,4′-Bipy (0.5 mmol, 0.078 g) was dissolved in 10 mL of ethanol, and it was mixed slowly with the previous solution. Within a few minutes, a white precipitate appeared, which was collected by filtration. Yield: 75%. IR: 3410(b), 2927(w), 2853(w), 1720(s), 1642(br), 1612(s), 1510(br), 1472(s), 1457(w), 1435(w), 1419(w), 1402(w), 1301(w), 1282(w), 1245(w), 1137(w), 1068(w), 807(w), 688(w), 611(w), 561(w), 527(w), 524(w). Anal. Calcd for salt 3: C 32.10% (32.05% theor); H 2.11% (2.07% theor); N 4.23% (4.16% theor).

Synthesis of salt 4 {(C₈Br₄O₄)^{2−}·2(C₅H₅N₂)⁺·2(H₂O)}. TBTA (0.5 mmol, 0.241 g) was dissolved in 10 mL of ethanol–water (1:1, v/v) mixture. The solution was stirred for 30 min. 3-AP (1 mmol, 0.095 g)

was dissolved in 10 mL of ethanol. Then the two solutions were slowly mixed with each other and kept in open air undisturbed. After 1 week, colorless block shaped crystals suitable for X-ray diffraction were collected. Yield: 60%. IR: 3505(w), 3437(b), 3414(w), 2924(w), 2843(w), 1712(s), 1645(br), 1611(s), 1504(br), 1467(s), 1438(w), 1421(w), 1408(s), 1307(w), 1279(w), 1241(w), 1133(w), 1058(w), 809(w), 681(w), 608(w), 556(w), 523(w), 517(w). Anal. Calcd for salt 4: C 30.60% (30.59% theor); H 2.61% (2.55% theor); N 7.91% (7.93% theor).

Synthesis of Co-crystal 5 $\{(\text{C}_8\text{H}_2\text{Br}_4\text{O}_4) \cdot (\text{C}_{12}\text{H}_8\text{N}_6) \cdot 2(\text{H}_2\text{O})\}$. TBTA (0.5 mmol, 0.241 g) was dissolved in 10 mL of ethanol–water (1:1, v/v) mixture. The solution was stirred for 30 min. DPTZ (0.5 mmol, 0.118 g) was dissolved in 10 mL of ethanol, and it was mixed slowly with the first solution. After another 30 min stirring, the resultant clear red color solution was allowed to evaporate under ambient temperature. After few days, red block shaped crystals suitable for X-ray single crystal diffraction were obtained. Yield: 60%. IR: 3410(b), 2922(w), 2853(w), 1716(s), 1637(br), 1610(vs), 1514(br), 1477(s), 1452(w), 1431(w), 1415(w), 1401(s), 1307(w), 1278(w), 1237(w), 1132(w), 1064(w), 801(w), 683(w), 610(w), 559(w), 517(w). Anal. Calcd for co-crystal 5: C 31.90% (31.86% theor); H 1.85% (1.86% theor); N 11.18% (11.14% theor).

Synthesis of Co-crystal 6 $\{(\text{C}_8\text{H}_2\text{Br}_4\text{O}_4) \cdot 2(\text{C}_5\text{H}_4\text{IN})\}$. This synthesis process is similar to that of the salt 4 except we have used 1 mmol of 3-iodopyridine (0.205 g) instead of 3-aminopyridine. Light yellow crystals were obtained after 10 days and characterized by single crystal X-ray diffraction technique. Yield: 60%. IR: 3417(b), 2924(w), 2848(w), 1719(s), 1643(br), 1614(s), 1509(br), 1462(s), 1438(w), 1425(w), 1407(s), 1317(s), 1289(w), 1248(w), 1139(w), 1055(w), 803(w), 685(w), 603(w), 552(w), 521(w). Anal. Calcd for co-crystal 6: C 24.25% (24.22% theor); H 1.10% (1.12% theor); N 3.18% (3.14% theor).

Powder X-ray Diffraction Analysis: Data Collection and Refinement. Powder X-ray diffraction data were collected at ambient temperature (20 °C) on a Bruker D8 Advance diffractometer operating in the reflection mode using Cu K α radiation having wavelength 1.5418 Å. The generator was set at 40 kV and 40 mA. For compounds 1 and 3, the PXRD data were collected within 2θ range of 5° – 70° (step size 0.02°) at scan speed 6 s/step. To check the phase purity, PXRD data of the compounds 2, 4, 5, and 6 were collected within 2θ range of 5° – 40° (step size 0.02°) at scan speed 0.5 s/step.

The powder X-ray diffraction patterns of 1 and 3 were indexed using the program *TREOR 90*¹⁶ of the *Fullprof.2k* package.¹⁷ The indexing reveals that 1 crystallizes in a monoclinic system with $a = 8.039(3)$ Å, $b = 10.325(5)$ Å, $c = 7.104(6)$ Å, and $\beta = 99.56(6)^\circ$ [$M(20) = 37$, $F(20) = 49$ (0.005847, 70)] and 3 crystallizes in a triclinic crystal system with $a = 6.493(5)$ Å, $b = 9.245(6)$ Å, $c = 9.971(6)$ Å, $\alpha = 64.061(13)^\circ$, $\beta = 85.752(11)^\circ$, and $\gamma = 73.662(16)^\circ$ [$M(20) = 19$, $F(20) = 34$ (0.010323, 58)]. The space groups were obtained from statistical analysis of the powder patterns with the help of the *findspace* module of the *EXPO 2009* software package.¹⁸ The statistical analysis shows that the most probable space groups of 1 and 3 are *C2/m* and *P1*, respectively. For these unit cells and space groups, full pattern decompositions were performed using Le Bail method giving good fit between calculated and experimental powder X-ray patterns.

The structure solutions from PXRD data were carried out using the simulated annealing technique (parallel tempering mode) as implemented in the program FOX,¹⁹ a Monte Carlo based software. The initial molecules were first drawn in ACD/ChemSketch, and the geometries of the molecules were optimized with the help of the MOPAC 2009²⁰ to get the reference structural model. For 1, a full TBTA molecule was taken initially as trial structural model, but after a few cycles, the optimization diverged, and the overlapping of the atoms was observed. We have faced with the same problem by taking half of the molecule. The optimization was successfully carried out by taking one-fourth of the molecule. During structure refinement, we have kept the position of the C4 atom fixed for unambiguous determination of structure through convergence of the refinement process with physically meaningful structural parameters. Similarly, for 3, the optimization process converges properly when we considered half TBTA, half 4,4'-bipy, and one guest water molecule as a reference structural model. The atomic coordinates

obtained from FOX were used as the starting model for the Rietveld structure refinement using the program GSAS²¹ with an EXPGUI²² interface. The peak shapes were described as pseudo-Voigt functions, and the backgrounds were fitted by the shifted Chebyshev function of first kind with 36 points regularly distributed over the entire 2θ range. Initially the lattice parameters, profile parameters, and background coefficients were refined. Soft constraints on bond lengths and bond angles and planar restraints on the aromatic rings were applied. A fixed isotropic displacement parameter of 0.04 \AA^2 for non-hydrogen atoms and 0.06 \AA^2 for hydrogen atoms was maintained. At the final stage of the refinement, preferred orientation correction was applied using the generalized spherical harmonic model. The Rietveld refinement yielded good fit with $R_p = 2.01\%$, $R_{wp} = 3.01\%$ for 1 and $R_p = 2.74\%$, $R_{wp} = 4.04\%$ for 3. The final crystallographic data and refinement parameters for 1 and 3 are depicted in Table 1.

Table 1. Crystallographic Data and Refinement Parameters of 1 and 3

	1	3
formula	$\text{C}_8\text{H}_2\text{Br}_4\text{O}_4$	$\text{C}_8\text{Br}_4\text{O}_4, \text{C}_{10}\text{H}_{10}\text{N}_2, 2(\text{H}_2\text{O})$
formula wt	481.70	673.91
cryst syst	monoclinic	triclinic
space group	<i>C2/m</i>	<i>P1</i>
<i>a</i> , Å	8.0299(9)	6.4938(7)
<i>b</i> , Å	10.3117(11)	9.2279(9)
<i>c</i> , Å	7.0948(8)	9.9675(10)
α , deg	90	64.0531(10)
β , deg	99.5592(11)	85.7704(13)
γ , deg	90	73.6886(13)
<i>V</i> , Å ³	579.31(11)	514.63(9)
<i>Z</i>	2	1
<i>Z'</i>	0.25	0.5
ρ_{calc} g cm ^{−3}	2.761	2.174
temp, K	293	293
2θ range, deg	5.0–70.0	5.0–70.0
R_{wp}	0.03	0.04
R_p	0.02	0.03
R_F^2	0.03	0.16
χ	2.16	4.80

Single Crystal X-ray Diffraction Analysis: Crystallographic Data Collection and Refinement. Suitable single crystals of 2, 4, 5, and 6 were mounted on a Bruker SMART diffractometer equipped with a graphite monochromator and Mo K α ($\lambda = 0.71073$ Å) radiation. The structures were solved by using the SHELXS 97. Subsequent difference Fourier synthesis and least-squares refinement revealed the positions of the remaining non-hydrogen atoms. Non-hydrogen atoms were refined with independent anisotropic displacement parameters. Hydrogen atoms were placed in idealized positions, and their displacement parameters were fixed to be 1.2 times larger than those of the attached non-hydrogen atoms. Successful convergence was indicated by the maximum shift/error of 0.001 for the last cycle of the least-squares refinement. All calculations were carried out using SHELXL 97,²³ SHELXS 97,²⁴ PLATON 99,²⁵ ORTEP-3,²⁶ and WinGX system Ver-1.64.²⁷ All crystallographic data for the compounds (2, 4, 5, and 6) are summarized in Table 2. Noncovalent interactions are summarized in Tables S1–S11, Supporting Information.

Hirshfeld Surface Analysis. The Hirshfeld surface²⁸ is defined as the outline of the shape occupied by a molecule in the crystal structure and is constructed based on the electron distribution²⁹ calculated as the sum of spherical atom electron densities. Two-dimensional fingerprint plots³⁰ are obtained by Hirshfeld surface analysis not only to identify each type of intermolecular interaction but also to provide the relative area of the surface corresponding to each kind of interaction. Hirshfeld surfaces and the associated 2D-fingerprint plots were calculated by using Crystal Explorer 3.0,³¹ which accepts a structure input file in CIF format.

Table 2. Crystallographic Data and Refinement Parameters of 2 and 4–6

	2	4	5	6
formula	C ₈ H ₂ Br ₄ O ₄ · 2(H ₂ O)	C ₈ Br ₄ O ₄ · 2(C ₅ H ₇ N ₂), 2(H ₂ O)	C ₈ H ₂ Br ₄ O ₄ · C ₁₂ H ₈ N ₆ · 2(H ₂ O)	C ₈ H ₂ Br ₄ O ₄ · 2(C ₅ H ₄ IN)
formula wt	517.77	706.00	754.01	891.68
cryst syst	monoclinic	monoclinic	triclinic	triclinic
space group	P2 ₁ /n	P2 ₁ /c	P $\bar{1}$	P $\bar{1}$
a, Å	5.8277(6)	9.2517(3)	8.4983(5)	6.8225(5)
b, Å	14.727(2)	7.0646(2)	8.7073(4)	8.9985(6)
c, Å	16.5226(19)	18.7083(7)	9.9547(5)	10.1541(7)
α, deg	90	90	92.062(2)	96.117(4)
β, deg	97.177(5)	101.565(2)	112.550(3)	90.172(4)
γ, deg	90	90	114.459(2)	106.548(4)
V, Å ³	1406.9(3)	1197.94(7)	602.40(6)	593.80(7)
Z	4	2	1	1
Z'	1	0.5	0.5	0.5
ρ _{calc} , g cm ^{−3}	2.444	1.957	2.078	2.494
μ, mm ^{−1}	11.455	6.760	6.732	9.404
F(000)	968	684	364	410
cryst size, mm ³	0.12 × 0.16 × 0.18	0.16 × 0.18 × 0.22	0.12 × 0.16 × 0.18	0.12 × 0.16 × 0.19
temp, K	100	293	296	293
θ _{min} /θ _{max} , deg	1.9/24.7	2.2/28.2	2.6/32.5	2.0/30.7
total/unique reflns	5368/2358	12818/2962	8112/4204	10691/3565
R _{int}	0.16	0.06	0.07	0.11
obsd data [I > 2σ(I)]	894	1493	3067	1190
N _{ref} /N _{par}	2358/158	2962/148	4204/184	3565/127
R	0.08	0.06	0.04	0.07
wR2	0.18	0.17	0.10	0.18
S	0.81	1.05	1.01	0.92

Bond lengths to hydrogen atoms were set to typical values obtained from neutron diffraction data (C–H = 1.083 Å, N–H = 1.009 Å, and O–H = 0.938 Å). For each point on the Hirshfeld isosurface, if d_e is the distance from the point to the nearest nucleus external to the surface and d_i is the distance of the nearest nucleus internal to the surface, then the normalized contact distance (d_{norm}) is given by

$$d_{\text{norm}} = \frac{(d_i - r_i^{\text{vdW}})}{r_i^{\text{vdW}}} + \frac{(d_e - r_e^{\text{vdW}})}{r_e^{\text{vdW}}}$$

where r_i^{vdW} and r_e^{vdW} are the van der Waals radii of the appropriate atoms internal and external to the surface, respectively. The value of d_{norm} is negative or positive depending on intermolecular contacts being shorter or longer than the van der Waals separations. When calculations are over, then the parameter d_{norm} constructs a surface with a red–white–blue color scheme, where bright red spots highlight shorter contacts, white areas represent contacts around the van der Waals separation, and blue regions are for the longer contacts.

Computational Details of Theoretical Analysis. The theoretical energy calculation of 1–6 in gas phase was performed by Gaussian 03 software package.³² For this particular purpose, the analytical gradient methods of DFT with Becke's three parameters (B3) exchange functional together with the Lee–Yang–Parr (LYP) nonlocal correlation functional (symbolized as B3LYP) was employed. We have chosen 6-31G(d,p) basis set for 1–5, whereas for 6 calculations have carried out using the basis set LanL2DZ, having an effective core potential.

Device Fabrication and Current–Voltage (*I*–*V*) Measurement. *I*–*V* measurement has been carried out on an “ITO/sample/Al” sandwich structure (ITO = indium–tin oxide and sample = compound 3). Primarily, the sample was dispersed in DMF by vigorous ultrasonication, then the dispersion was poured dropwise onto an ITO coated glass slide placed on the platform of a spin coating unit (SCU-2007). A uniform thin film of the sample was deposited on the ITO coated glass slide by spin coating for 3 min at 1600 rpm. Afterward the film was heated under vacuum at 80 °C for 10 min to evaporate the solvent from the deposited film. Thereafter, an Al electrode was deposited onto the composite film using ashadow mask by vacuum thermal evaporation, with the help of

12A4D HHV vacuum coating unit. The effective contact area of the device is $7.065 \times 10^{-3} \text{ cm}^2$. The room temperature (at 300 K) current–voltage (*I*–*V*) characteristics were measured using a Keithley 2400 sourcemeter, interfaced with a PC by applying bias voltage in the range of +1 to −1 V.

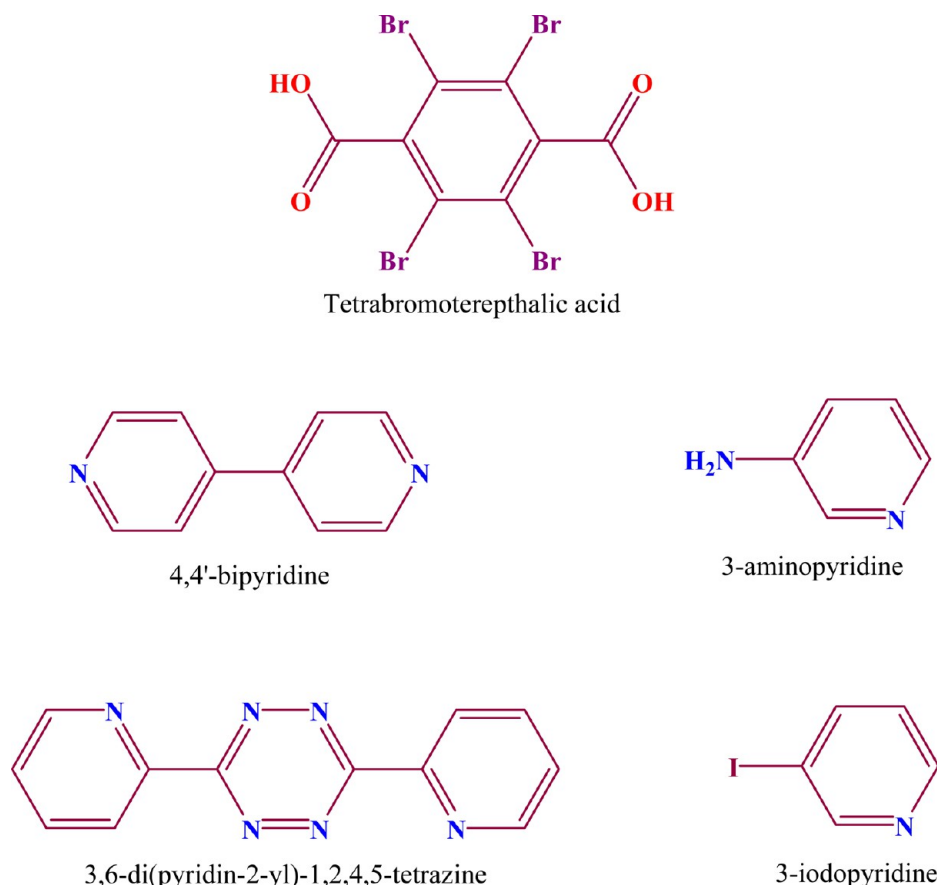
RESULTS AND DISCUSSION

The molecular structures of TBTA, 4,4'-bipyridine, 3-aminopyridine, 3,6-di(pyridin-2-yl)-1,2,4,5-tetrazine, and 3-iodopyridine are depicted in Scheme 1. Because of the presence of pro-efficient –COOH group and π rings, TBTA has been chosen as the co-crystal/salt forming agent with organic bases. Here, we are going to describe the crystal structure of TBTA (1), hydrated-TBTA (2), two salts of TBTA (3 and 4), and two co-crystals of TBTA (5 and 6). Among these, the crystals structure of TBTA^{2−}–4,4'-bipy²⁺ (3) was previously reported.³³ We have solved the crystal structures of TBTA (1) and TBTA^{2−}–4,4'-bipy²⁺ (3) from powder X-ray diffraction data, and the corresponding Rietveld plots are presented in Figure 1a,b.

Molecular and Supramolecular Structure of 1. Powder X-ray diffraction data analysis reveals that 1 crystallizes in a monoclinic system with space group C2/*m*. The asymmetric unit of 1 contains one fourth of a TBTA molecule (Figure S1, Supporting Information), that is, two carboxylic oxygen atoms, two carbon atoms with multiplicity four, and one carbon atom and one bromine atom with multiplicity eight. In the molecular structure, two carboxylic groups are parallel to each other, and they are exactly perpendicular to the aromatic ring of the TBTA molecule.

The crystal packing of 1 indicates that two TBTA molecules are connected by supramolecular O–H...Br hydrogen bonding interactions. The overall structure is a 2D supramolecular sheet (Figure 2), which is created by the supramolecular bifurcated O2–H2...Br1 (3.27 Å) and O2–H2...Br1* (3.27 Å) (* = −*x*, *y*, −*z*)

Scheme 1. Molecular Structures of Tetrabromoterephthalic Acid, 4,4'-Bipyridine, 3-Aminopyridine, 3,6-Di(pyridine-2-yl)-1,2,4,5-tetrazine, and 3-Iodopyridine



hydrogen bonding interactions. Within the 2D sheet, two types of homosynthon are observed with Etter graph set notations³⁴ $R^2_2(12)$ and $R^4_2(10)$. Usually, carboxylic acids show $R^2_2(8)$ type homosynths by forming carboxylic acid dimers, but here unusual weak hydrogen bond formation takes place due to the presence of the bromide group. There is a competition between the weak and strong hydrogen bonding interactions, and in this case, strong hydrogen bonding interactions are defeated by weak hydrogen bonds. All hydrogen bonding interactions of **1** are presented in Table S1, Supporting Information.

Molecular and Supramolecular Structure of Hydrate **2**.

SC-XRD analysis reveals that **2** crystallizes in a monoclinic system with space group $P2_1/n$, and its asymmetric unit contains one TBTA molecule and two solvent water molecules (Figure S2, Supporting Information). The molecular structure of TBTA is almost identical to that of **1**. The $-\text{COOH}$ functional groups of TBTA display two nonequivalent C–O bonds, a shorter one exhibiting double bond ($\text{C}=\text{O}$) character and a longer single bond (C–O) with a protonated oxygen atom (O1 and O4). These $-\text{COOH}$ functional groups are twisted about C–C bond against the aromatic ring. The torsion angles represented by C2–C1–C7–O2 and C3–C4–C8–O4 are $84(3)^\circ$ and $92(3)^\circ$, respectively.

In this crystal structure, the TBTA molecule acts as hydrogen bond donor as well as acceptor. Two carboxylic acid groups of the TBTA molecule are connected with two different solvent water molecules by O1–H1 \cdots O2W (2.52 Å) and O4–H1O4 \cdots O1W (2.59 Å) hydrogen bonding interactions. Again they are connected via supramolecular O1W–H2W1 \cdots O3 (2.81 Å) and

O2W–H2W2 \cdots O2 (2.76 Å) hydrogen bonding interactions. Furthermore, two water molecules are linked by supramolecular O2W–H1W2 \cdots O1W (2.72 Å) hydrogen bonding interactions. The overall 3D supramolecular structure (Figure 3) is formed by the above-mentioned hydrogen bonding interactions, and this 3D supramolecular structure gets additional stability with the assistance of supramolecular C1–O1 $\cdots\pi$ interactions (Figure S3, Supporting Information). All hydrogen bonding and $\pi\cdots$ interactions of **2** are listed in Tables S2 and S3, Supporting Information.

Molecular and Supramolecular Structure of Salt (**3**).

Powder X-ray diffraction data analysis reveals that **3** crystallizes in a triclinic system, and statistical analysis reveals that it possesses a centrosymmetric space group $P\bar{1}$. The asymmetric unit of **3** contains half TBTA^{2−} anion, half 4,4'-bipy²⁺ cation, and a water molecule (Figure S4, Supporting Information). Two pyridine rings of 4,4'-bipy²⁺ are coplanar, and the torsion angle between the pyridine rings is almost 180° .

Two types of supramolecular interaction are observed in the crystal packing of **3**: hydrogen bonding and $\pi\cdots$ interactions. The hydrogen bonding interaction between TBTA^{2−} and 4,4'-bipy²⁺ ions leads to the formation of 1D supramolecular chain through N1⁺–H1 \cdots O1[−] (2.582 Å) heterosynthon with Etter graph set notation $C_2^2(18)$. These 1D chains are further connected with solvent water molecules by O1W–H1W1 \cdots O2 (2.80 Å) and O1W–H2W1 \cdots O2 (2.80 Å) hydrogen bonds leading to the formation of 2D supramolecular sheet structure (Figure 4). The $\pi\cdots\pi$ and Br $\cdots\pi$ interactions connect the 2D supramolecular sheets to form a 3D supramolecular network (Figure S5,

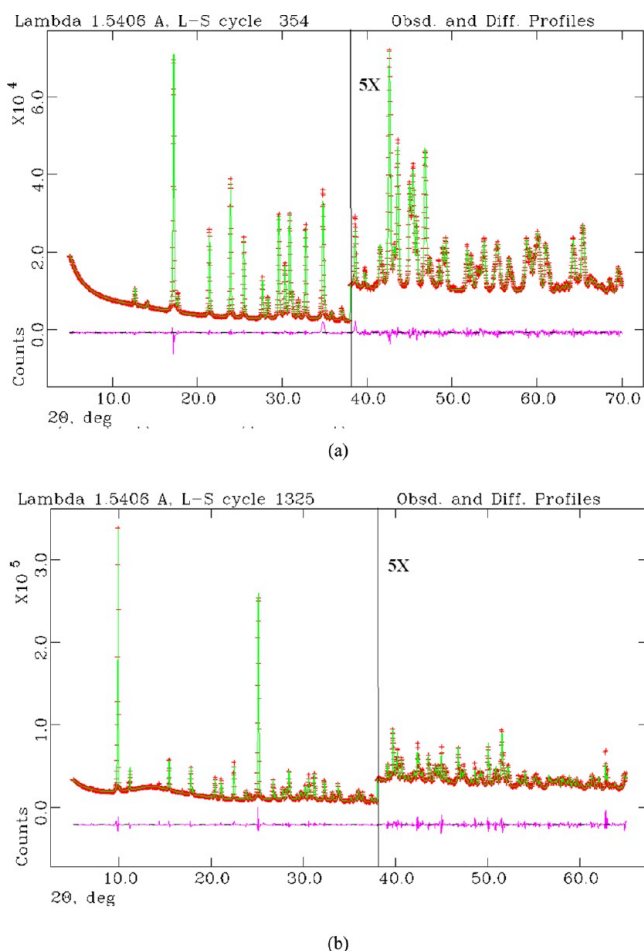


Figure 1. Rietveld plots for (a) 1 and (b) 3.

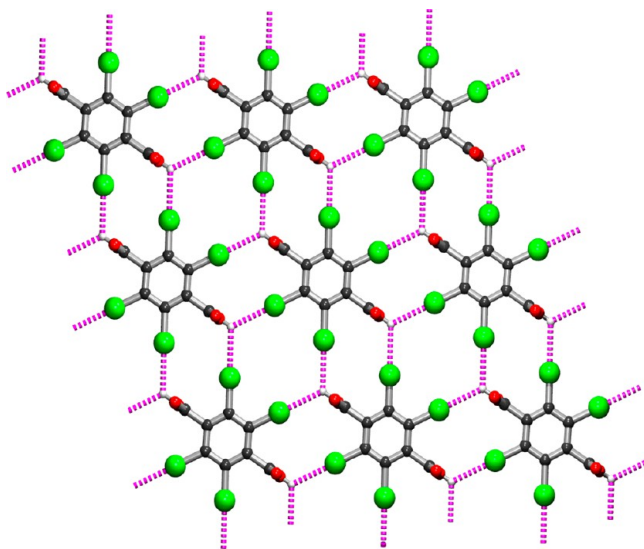


Figure 2. Two-dimensional supramolecular sheet structure formed by O—H...Br hydrogen bonding interactions for 1.

Supporting Information). All hydrogen bonding and $\pi\cdots$ interactions of 3 are summarized in Tables S4 and S5, Supporting Information.

Molecular and Supramolecular Structure of Salt (4). TBTA and 3-AP form a salt that crystallizes in monoclinic system with space group $P2_1/c$ with half $TBTA^{2-}$ ion, one $3-AP^+$ ion, and

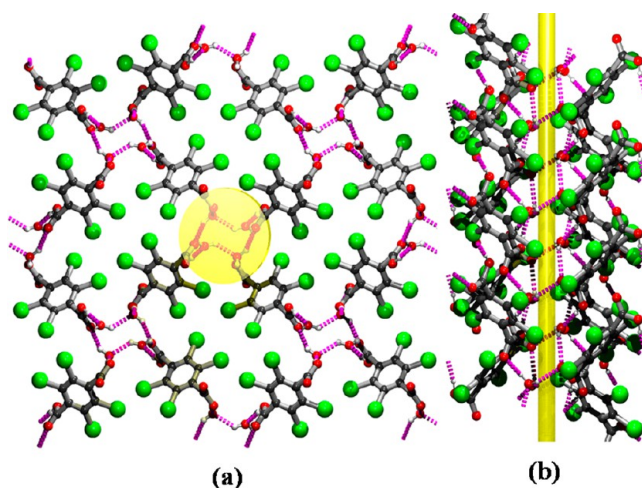


Figure 3. (a) Three-dimensional supramolecular structure formed by water mediated hydrogen bonding interactions and (b) helical 1D supramolecular chain formed in 2.

one water molecule in the asymmetric unit (Figure S6, Supporting Information). In the unit cell of 4, the $TBTA^{2-}$ ion adopts a similar molecular geometry as that observed in 3. The transfer of protons from the TBTA molecule to the 3-AP molecule was confirmed by single crystal structure analysis. The Fourier map (obtained during structural refinement) has revealed that the C—O bond distances (C7—O1 = 1.26 Å and C4—O2 = 1.23 Å) are not equal to each other and also they do not match with the standard value of C—O(H) bond. It may therefore be concluded that proton transfer takes place during crystallization.

Here, $3-AP^+$ engages itself in supramolecular hydrogen bonding interactions due to the presence of the pyridine group and the amino group. The pyridine nitrogen is protonated, and as a result of this it takes part in a charge assisted $N^+-H\cdots O^-$ (2.62 Å) hydrogen bonding interaction with the $TBTA^{2-}$ ion. One $TBTA^{2-}$ ion is linked with two $3-AP^+$ ions leading to the formation of a supramolecular trimer (Figure 5). These trimers are bridged through water mediated hydrogen bonding interactions N1—H1A...O1W (2.89 Å), N1—H2B...O1W (2.86 Å), O1W—H1W1...O1 (2.75 Å), and O1W—H2W1...O2 (2.75 Å) leading to the formation of a 3D supramolecular structure (Figure 6). The overall 3D supramolecular structure formation is also facilitated by weak $Br\cdots\pi$ interactions (Figure S7, Supporting Information). All hydrogen bonding and $\pi\cdots$ interactions of 4 are presented in Tables S6 and S7, Supporting Information.

It is interesting to note that in the present crystal structure the water molecule (O1W) acts as double hydrogen bond donor as well as double hydrogen bond acceptor and thus formation of a tetrahedral synthon motif (Figure S8, Supporting Information) takes place.

Molecular and Supramolecular Structure of Co-crystal (5). The single crystal structure analysis reveals that the co-crystal (5) crystallizes in the triclinic system with centrosymmetric space group $P\bar{1}$. Its asymmetric unit contains half TBTA, half DPTZ, and a solvent water molecule (Figure S9, Supporting Information). In the unit cell of 5, the TBTA molecule adopts a molecular conformation similar to that of TBTA in 1 and 2. The DPTZ molecule has three aromatic rings: two pyridine rings and one tetrazine ring. The two pyridine rings are almost coplanar with each other, and they are inclined with the central aromatic ring, where the torsion angles between the pyridine rings and the central ring are 19.2° (N1—C9—C10—N2) and 17.9° (C8—C9—C10—N3).

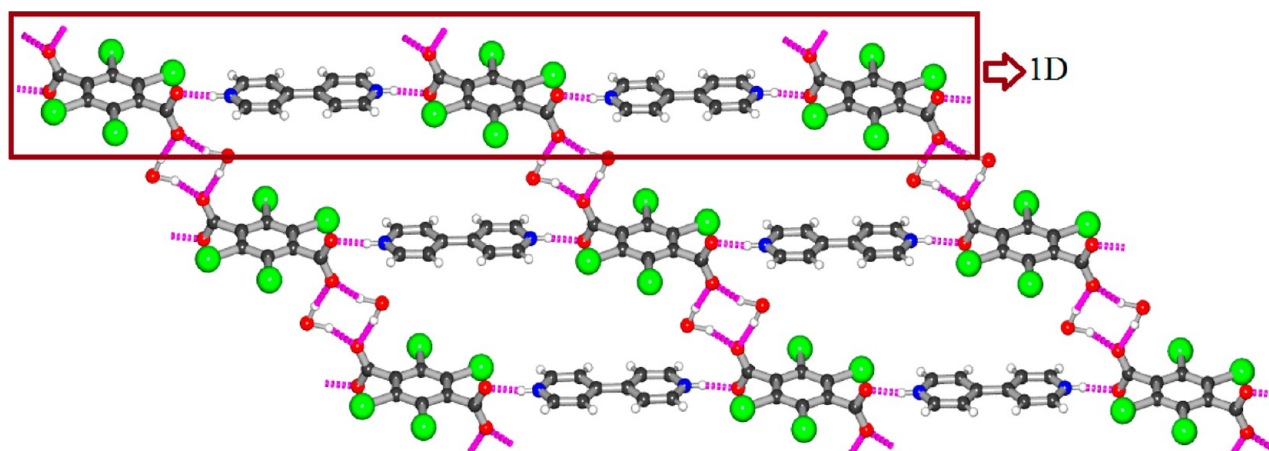


Figure 4. Two-dimensional supramolecular sheet structure formed by water mediated hydrogen bonding interactions in 3.

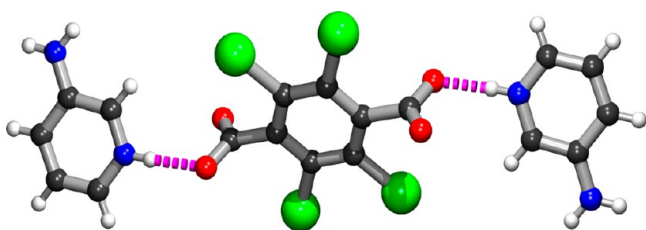


Figure 5. Supramolecular trimer formation through hydrogen bonding interactions in 4.

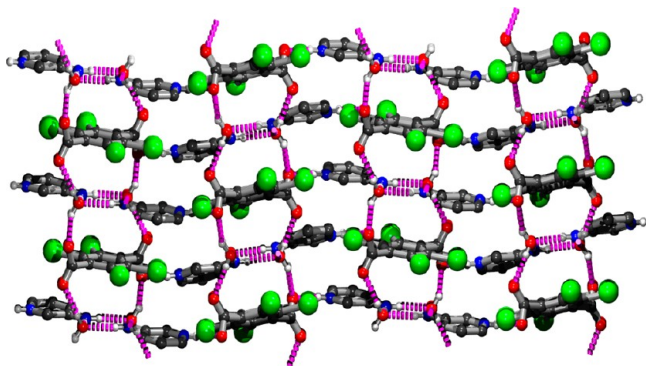


Figure 6. Three-dimensional supramolecular structure formation through water mediated hydrogen bonding interactions in 4.

Unlike 3 and 4, in case of 5 no proton transfer occurs from the $-\text{COOH}$ group of TBTA to the pyridine ring of the DPTZ molecule. The C–O bond lengths [$\text{O1}-\text{C4} = 1.306(3) \text{ \AA}$, $\text{O2}-\text{C4} = 1.200(3) \text{ \AA}$] confirm the existence of an acid group ($-\text{COOH}$ group).

The neutral TBTA and DPTZ molecules are not connected directly by hydrogen bonds, but they are linked through water mediated hydrogen bonding interactions. The TBTA molecule is connected with a water molecule via the $\text{O1}-\text{H1}\cdots\text{O1W}$ (2.56 \AA) hydrogen bonding interaction, and furthermore the water molecule is linked with the DPTZ molecule through bifurcated $\text{O1W}-\text{H1W1}\cdots\text{N1}$ (2.81 \AA) and $\text{O1W}-\text{H1W1}\cdots\text{N2}$ (3.09 \AA) hydrogen bonding interactions leading to the formation of a 2D supramolecular sheet within the crystallographic ac -plane (Figure 7). These 2D supramolecular sheets are further connected by supramolecular $\pi\cdots\pi$ and $\text{O}\cdots\pi$ interactions leading to the formation of a 3D supramolecular network (Figure 8 and

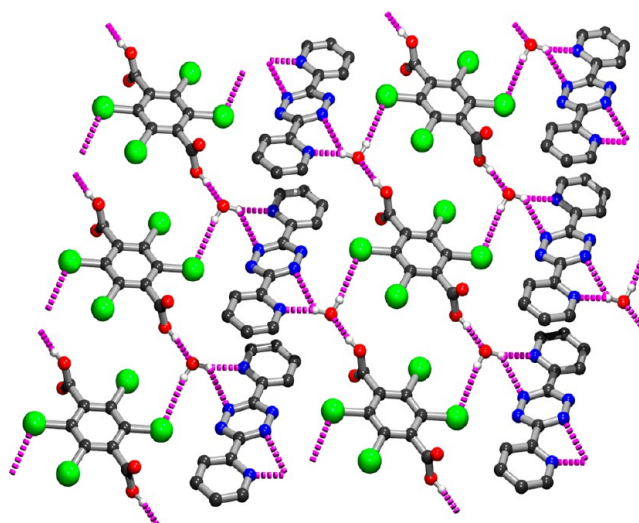


Figure 7. Two-dimensional supramolecular sheet structure formation takes place through hydrogen bonding interactions of 5.

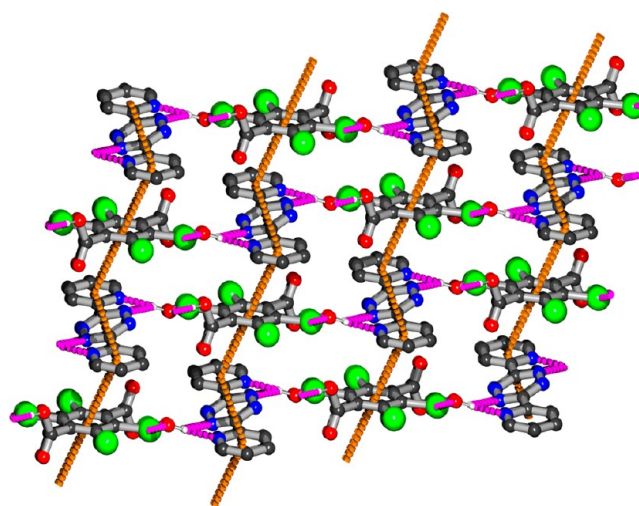


Figure 8. Three-dimensional supramolecular structure formation takes place through hydrogen bonding (magenta) and $\pi\cdots\pi$ interactions (orange) in 5.

Figure S10, Supporting Information). All hydrogen bonding and $\pi\cdots\pi$ interactions of 5 are listed in Tables S8 and S9, Supporting Information.

Molecular and Supramolecular Structure of 6. The single crystal structure analysis reveals that co-crystal **6** crystallizes in a triclinic system with centrosymmetric space group $P\bar{1}$. The asymmetric unit contains half TBTA and one 3-IP molecule (Figure S11, Supporting Information). The single crystal X-ray structure analysis confirms the presence of both C–O and C=O [1.305(14) Å (C10–O2) and 1.191(12) Å (C10–O1)], which suggests that the TBTA molecule in the crystal structure of **6** is neutral. In co-crystal **6**, the carboxylic groups (–COOH) are almost perpendicular with the aromatic ring of TBTA, and the torsion angles represented by C8–C9–C10–O2 and C7*–C9–C10–O1 (* = 1 – x , 1 – y , 1 – z) are 90.6° and 96.3°, respectively.

As expected, the O–H...N hydrogen bonding interaction [O2–H2...N1 (2.60 Å)] is present between the carboxylic acid and the pyridine group. Using this hydrogen bonding interaction, each TBTA binds with two different 3-IP molecules and forms a supramolecular trimer (Figure S12, Supporting Information). In addition, one 3-IP molecule interacts with another 3-IP molecule through π ... π interactions to form supramolecular dimers, which are further connected by Br... π interactions with TBTA molecules leading to the formation of a supramolecular 1D chain (Figure 9). The O2–H2...N1 hydrogen bonding interaction



Figure 9. One-dimensional chain via π ... π and Br... π interactions of co-crystal **6**.

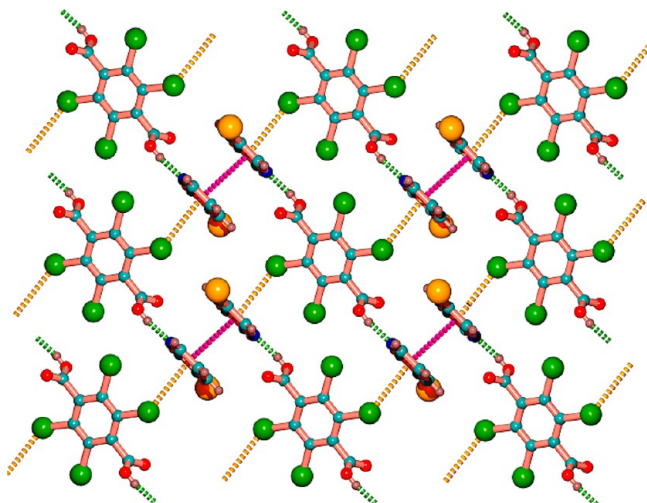


Figure 10. Two-dimensional sheet formed by supramolecular π ... π and Br... π interactions and O–H...N hydrogen bonding interactions of **6**.

connects these 1D supramolecular chains to form a 2D supramolecular sheet structure, Figure 10. This co-crystal also contains weak van der Waals interactions between iodine and carboxylate oxygen atoms (Figure S13, Supporting Information). All hydrogen bonding and π ... interactions of **6** are summarized in Tables S10 and S11, Supporting Information.

It should be noted that among the four multicomponent systems, **3**, **4**, and **5** contain solvent water molecules within their asymmetric unit in contrast to **6**. It has been found that salts have a higher tendency to form solvates than co-crystals.³⁵ This is because the charged species have more tendencies to form

hydrogen bonds and thus after formation of charge assisted hydrogen bonds they prefer to make hydrogen bonds with other neutral molecules such as solvents, acids, or bases. Here, both **3** and **4** are salts, and their supramolecular structure analyses reveal that both compounds form hydrogen bonds with solvent water after formation of charge assisted (O[–]...H–N⁺) hydrogen bonds between the acid–base pair.

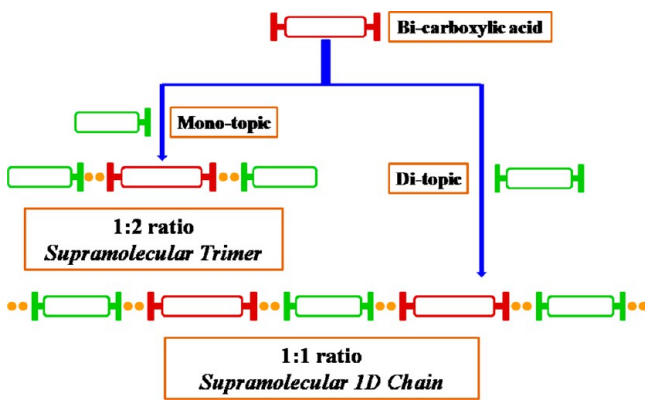
The significance of water in co-crystallization has been revealed by Aakeroy et al. and Zaworotko et al. recently.³⁶ According to Zaworotko et al., water molecules could help in stabilizing the crystal structure in a system with an imbalance in the number of donor and acceptor sites.^{36b} In our case, between co-crystals **5** and **6**, **5** contains solvent water molecules, while **6** does not. In **5**, the base molecule has six acceptor sites, and the acid molecule has two donor sites; thus there is a clear difference in the number of donor sites of acid and acceptor sites of base. In **5**, water molecules act as donor to the N atoms of tetrazine moiety and as acceptor for the carboxylic groups of TBTA. Though **5** contains both carboxylic acid and basic pyridyl groups, supramolecular structural analysis reveals the absence of so-called O–H...N hydrogen bonding interactions between the acid and base molecules; rather the acid–base molecules connect to each other through water mediated hydrogen bonding interactions. In contrast, supramolecular structural analysis of co-crystal **6** reveals that each TBTA molecule binds with two different 3-IP molecules through O–H...N hydrogen bonding interactions. Thus, following Zaworotko et al.,^{36b} it can be said that due to the difference in number of donor and acceptor sites between the acid and base molecules, there is a necessity of solvent water molecules to bridge between the acid and base molecules in **5** during crystallization. Hence in co-crystal **5**, solvent water molecules participate in co-crystallization, but in **6**, they do not.

It is to be noted that among these compounds, in **3**, **4**, and **5**, supramolecular interactions form a 3D supramolecular network, while in **6** a 2D supramolecular sheet structure forms. So, it is obvious that the water molecules play a significant role in stabilizing the crystal structure and extending the dimensionality of the supramolecular network.

After analyzing the molecular and supramolecular structure of the compounds, we have found that in **3** the acid–base ratio is 1:1, while in **4** and **6**, it is 1:2. The O–H...N hydrogen bonding interactions between acid–base lead to the formation of a 1D supramolecular chain for **3** and, on the other hand, supramolecular trimers for **4** and **6** (Scheme 2). TBTA is a bicarboxylic acid and thus can form two O–H...N or O[–]...H–N⁺ hydrogen bonds with base molecules. 4,4'-Bipyridine contains two nitrogen atoms and thus can form two O–H...N or O[–]...H–N⁺ hydrogen bonds. So, in **3**, the ratio of bicarboxylic TBTA and base 4,4'-bipyridine is 1:1. Each deprotonated bicarboxylic acid forms two O[–]...H–N⁺ hydrogen bonds with two different protonated 4,4'-bipyridines leading to the formation of a 1D supramolecular chain. In contrast, both 3-AP and 3-IP contain only one pyridyl group; therefore, they can form only one hydrogen bond using the pyridyl group. So, during co-crystallization, each deprotonated bicarboxylic acid binds with two protonated 3-AP⁺ in **4** and one bicarboxylic acid binds with two 3-IP molecules in **6** to form supramolecular trimers in each case. As a result, in both **4** and **6** the acid–base ratio is 1:2. So, based on number of donor–acceptor sites in the acid/base molecules, bicarboxylic acid molecules can form 1:1 and 1:2 acid–base co-crystals or salts.

Hirshfeld Surface Analysis. M. A. Spackman and co-workers have developed a tool, “Hirshfeld surface” with “2D fingerprint plot”, to elucidate the packing modes and intermolecular

Scheme 2. The Acid–Base Ratio within the Obtained Co-crystal or Salt Depends upon the Number of Donor–Acceptor Sites in the Acid and Base Molecules, Which Consequently Dictates the Formation of Supramolecular 1D Chain or Trimer through O–H⋯N/O⋯H–N⁺ Hydrogen Bonds



interactions in molecular crystals in a graphical format.^{29a} Hirshfeld surfaces reflect all intermolecular interactions, while 2D fingerprint plots reveal the nature and type of intermolecular interactions experienced by a “target” molecule in the bulk crystalline environment through a colored-graphical format. Here, we have performed Hirshfeld surfaces of the TBTA (target molecule) to establish how it interacts intermolecularly with other constituents of the crystal structure in the different crystalline environments of 1–6.

The Hirshfeld surfaces of TBTA in the crystal structures of 1–6 are shown in Figure 11, which displays the surfaces that have been mapped over a d_{norm} range of -0.264 to 1.153 Å for 1, -0.746 to 1.139 Å for 2, -0.679 to 1.005 Å for 3, -0.651 to 1.228 Å for 4, -0.686 to 1.138 Å for 5, and -0.650 to 1.150 Å for 6. The d_{norm} surface is used for the identification of closed intermolecular interactions. The deep red spots in the Hirshfeld surfaces appear mainly due to O–H⋯Br for 1, O–H⋯O for 2, and O⋯H–O or O[−]⋯H–N⁺ hydrogen bonding interactions for 3 and 4. The deep red spots in the Hirshfeld surfaces indicate O–H⋯O and O–H⋯N hydrogen bonding interactions for 5 and 6, respectively. The small extent of the area and light red color on the Hirshfeld surfaces indicate the presence of weaker and longer contacts. The 2D fingerprint plots of 1–6 showing relative contribution to the Hirshfeld surface area due to O⋯H/H⋯O and C⋯H/H⋯C are presented in Figure 12.

In the case of 1, the O–H⋯Br/Br⋯H–O intermolecular interactions comprise 21.0% of the Hirshfeld surface. These H⋯Br/Br⋯H interactions represent one of the closest contacts that appear as deep red spots in the Hirshfeld surface mapped with d_{norm} and also have emerged as blunt spikes in the 2D fingerprint plot (Figure 12). Although the crystal structure of 1 does not show any classical hydrogen bonding interactions, close contact H⋯O/O⋯H interactions cover 3.6% of the total Hirshfeld surface. Other than these, C⋯H interactions, which comprise 5.7% of the Hirshfeld surface, are also prominent.

The 2D fingerprint plots of 2 reveal that H⋯O/O⋯H interactions comprise 18.7% of the Hirshfeld surface and appear as a sharp spikes, as shown in Figure 12. These interactions can be recognized by the presence of a deep red circular spot in the d_{norm} surface (Figure 11). The C⋯H/H⋯C interactions cover 4.4% (light red spot in the d_{norm} surface) of the total Hirshfeld surface. Like 1, in this crystal structure a Br⋯H interaction is also

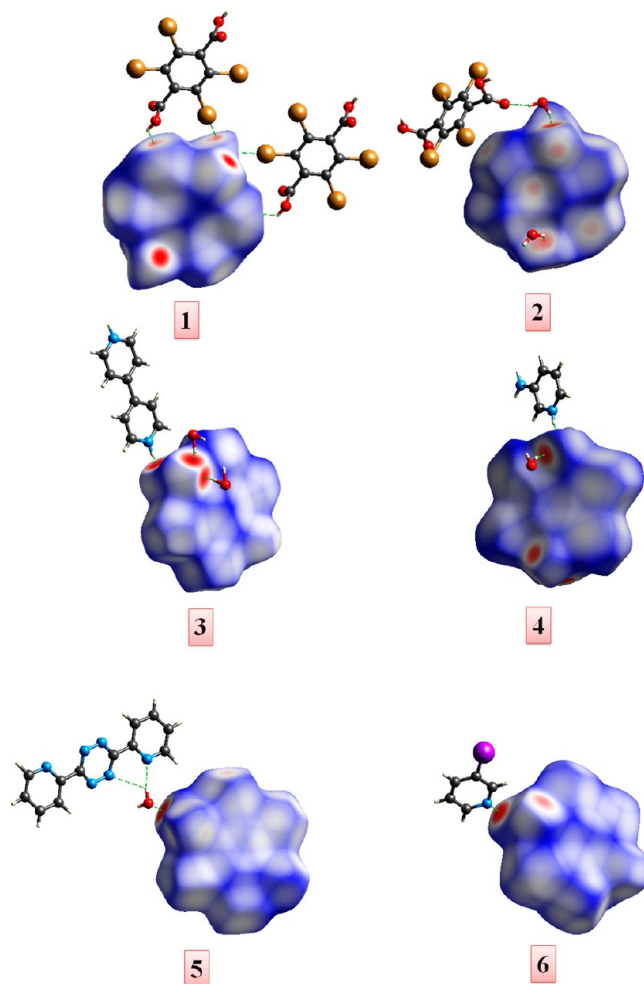


Figure 11. Hirshfeld surfaces of TBTA mapped over d_{norm} for the crystal structures of 1–6.

observed in the Hirshfeld surface, and it comprises only 6.3% of the total Hirshfeld surface.

The deep red circular spots in the Hirshfeld d_{norm} surface of TBTA^{2−} in 3 appear due to intermolecular O⋯H–N/N–H⋯O closed contacts. The 2D fingerprint plots of TBTA^{2−} in 3 reveal that the O⋯H interaction, which comprises 28.7% of the total surface, appears as a sharp spike with $d_i \approx 1.0$ Å and $d_e \approx 0.7$ Å (Figure 12). The C⋯H/H⋯C interactions cover 8.1% of the total Hirshfeld surface appeared as a light red spot in the d_{norm} surface. Like 1 and 2, here Br⋯H interactions are also present, and they contribute 22.5% of the total Hirshfeld surface.

The Hirshfeld surface of TBTA^{2−} ion in salt 4 shows two different types of deep red circular spots: one is due to the charge assisted O[−]⋯H–N⁺ hydrogen bonding interaction with the protonated 3-AP⁺ ion and other is due to the O⋯H–O hydrogen bonding interaction with the water molecule. The O⋯H interactions comprise 32.4% of the total Hirshfeld surface area and emerge in the 2D fingerprint plot as a sharp spike with $d_i \approx 1.1$ Å and $d_e \approx 0.7$ Å. The Br⋯H closed contact and C⋯H interaction cover 36.7% and 8.6% of the Hirshfeld surface, respectively.

The deep red circular spot in the Hirshfeld surface of TBTA in 5 can be attributed to the O–H⋯O hydrogen bonding interactions, and these have been observed in the 2D fingerprint plot as a sharp spike with $d_i \approx 0.7$ Å and $d_e \approx 1.0$ Å. The O⋯H–C close contact appears as a blunt spike in the 2D fingerprint plot

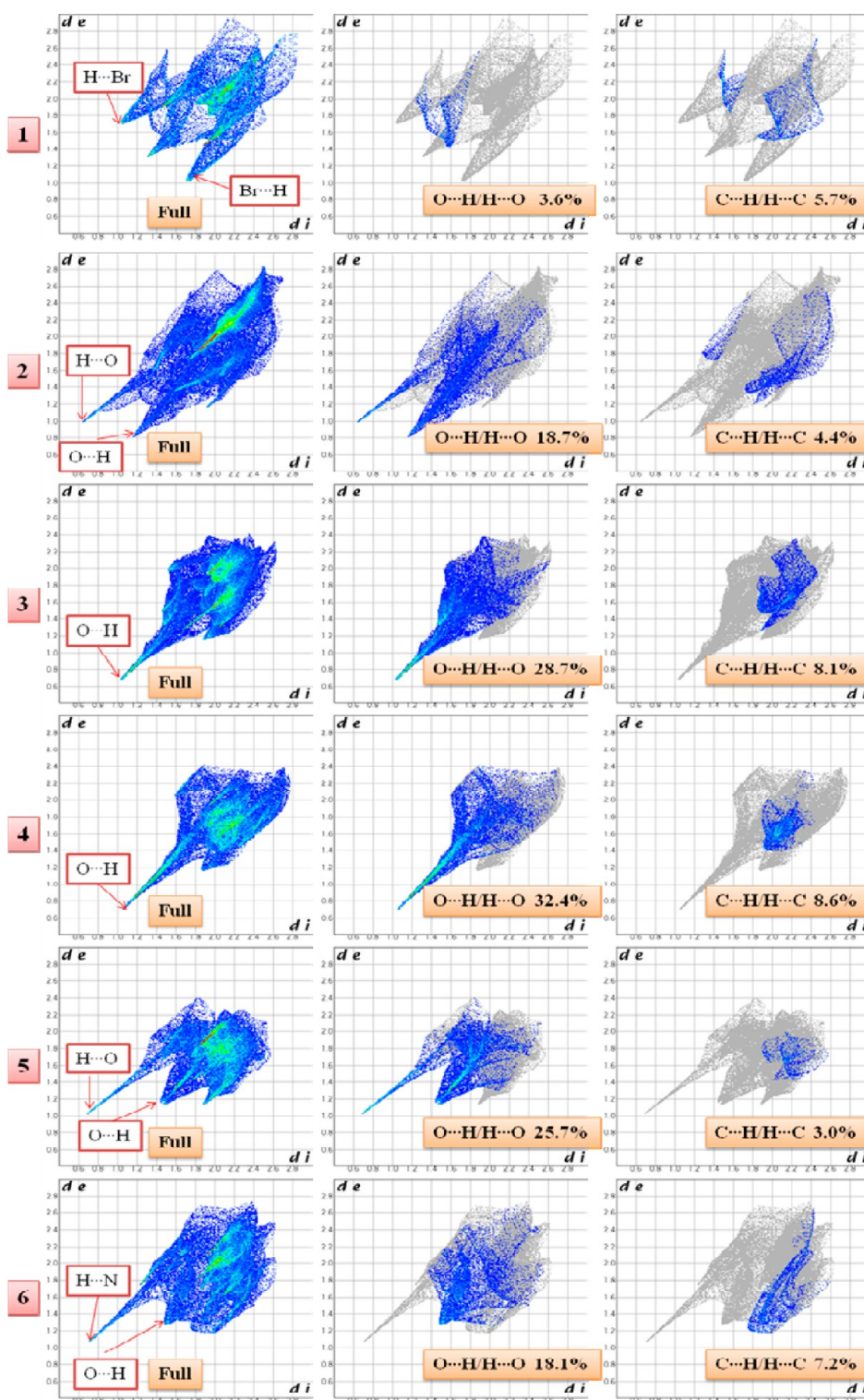


Figure 12. Fingerprint plots of 1–6: full plots (left) and plots resolved into O...H/H...O (middle) and C...H/H...C (right) contacts showing the percentages of contacts contributing to the total Hirshfeld surface area of TBTA.

with $d_i \approx 1.4$ Å and $d_e \approx 1.2$ Å. The O...H/H...O interactions comprise 25.7% of the total Hirshfeld surface. In **5**, Br...H close contacts are also present with 30.1% surface area of the total Hirshfeld surface, and these interactions appear in d_{norm} surface as pale red spots.

The 2D fingerprint plots of TBTA in **6** reveal that the O–H...N interaction comprises 5.4% of the Hirshfeld surface and

appears as a sharp spike with $d_i \approx 0.8$ Å and $d_e \approx 1.2$ Å (Figure 12). The deep red circular spot in the Hirshfeld d_{norm} surface can be attributed to O–H...N interactions (Figure 11). The H...O/O...H interactions cover 18.1% of the total Hirshfeld surface, and those have appeared as a narrow sharp blunt spike in the 2D fingerprint plot with $d_i = 1.5$ Å and $d_e = 1.3$ Å. Like **1**, **2**, **3**, **4**, and **5**, in this co-crystal Br...H interactions are observed in the Hirshfeld surface,

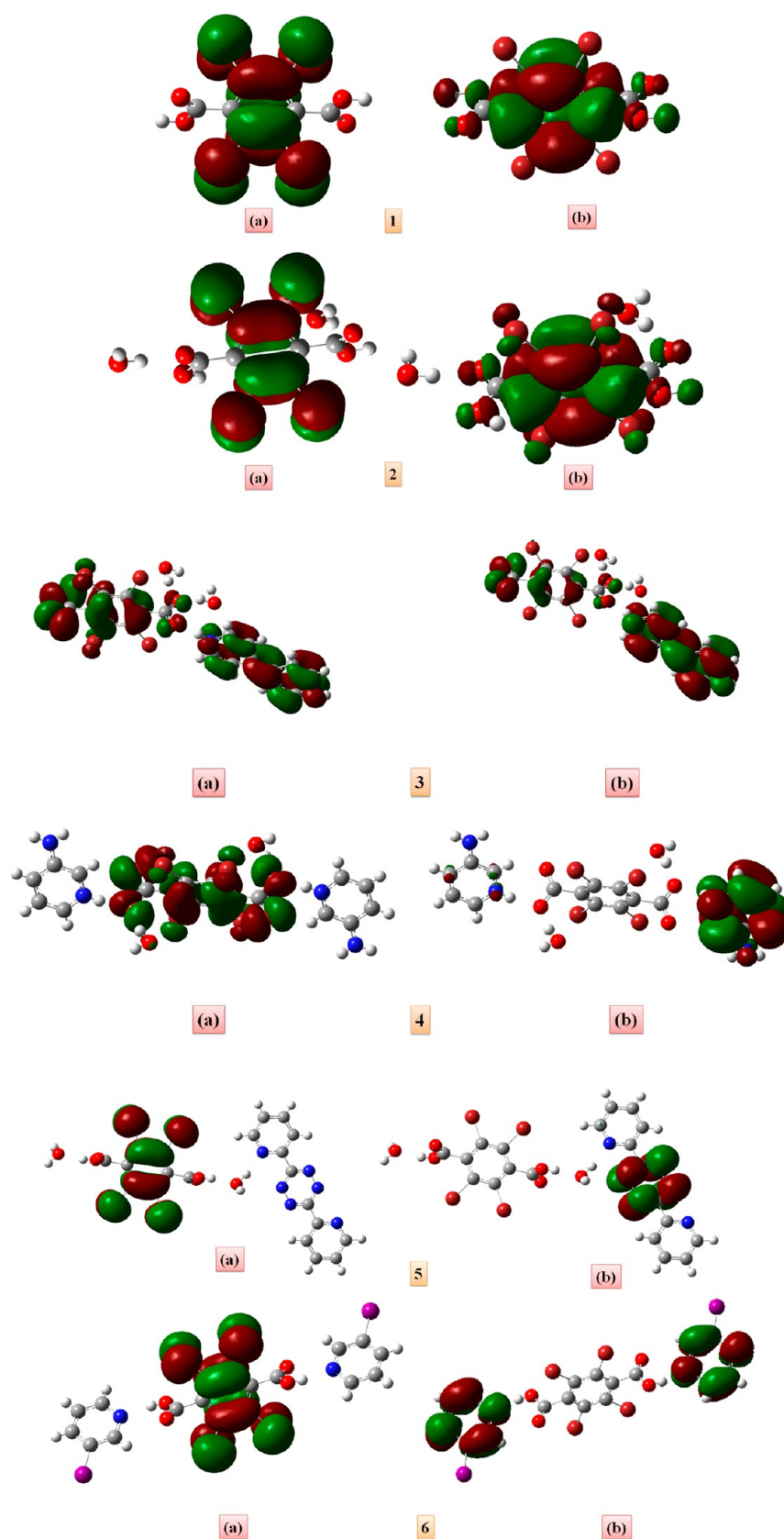


Figure 13. HOMO (a) and LUMO (b) of all compounds.

and they comprise 20.6% of the total Hirshfeld surface. The presence of another short interaction between iodine and oxygen atom ($I\cdots O$) is also prominent in the Hirshfeld d_{norm} surface.

The Hirshfeld surface analyses of the TBTA molecule in all the crystal structures reveal that the area occupied by $O\cdots H/H\cdots O$ hydrogen bonds is greater for the salt 4 than other crystal

structures indicating strong O···H/H···O hydrogen bonding interactions in the crystal packing of **4**. The single crystal structure analysis reveals that Br··· π interactions are present in all the crystal structures. The 2D fingerprint plots of TBTA in **1–6** corroborate this fact. The Br··· π interactions associated with Br···C interactions contribute 14.4%, 5.0%, 15.0%, 6.1%, 2.8%, and 15.7% of the entire Hirshfeld surface for **1–6**, respectively.

Theoretical Analysis. The optimized energies calculated by DFT method using B3LYP/6-31G (d,p) are −10840.4, −11046.62, −11541.6, −11653.5, −11836.79, and −1177.2 au for **1–6**, respectively. The highest occupied molecular orbitals (HOMOs) and lowest unoccupied molecular orbitals (LUMOs) are the main orbitals that take part in chemical stability. The HOMO represents the ability to donate an electron, and LUMO represents the ability to accept an electron. We have calculated the energy gap between HOMO and LUMO taking 6-31G(d,p) basis set for **1–5**, whereas for **6** calculations have been carried out using the basis set LanL2DZ, having an effective core potential. The HOMO–LUMO plots are depicted in Figure 13. The HOMO–LUMO energy gaps are 11.75, 4.63, 0.27, 1.49, 3.29, and 4.97 eV for **1–6**, respectively. These values are relatively high for **1**, **2**, **5**, and **6** indicating high stability, low electrical conductivity, and high chemical hardness for these samples. But the HOMO–LUMO gap for salts **3** and **4** are relatively low, indicating that the electrical conductivity of these compounds is higher compared with other compounds. This may be because in case of **3** and **4** charge transfer takes place from carboxylic acid to the pyridine molecule during crystallization.

Thermal Analysis. Thermal analyses of compounds **3**, **4**, **5**, and **6** were carried out in N₂ atmosphere at a heating rate of 10 °C min^{−1} in the temperature range of 25–500 °C (Figure S14, Supporting Information). Thermal plots show that mass loss occurs in two steps for **3**, **4**, and **5**, while for **6** it occurs in a single step. For **3**, **4**, and **5**, solvent water molecules are removed within 80–130 °C in all cases. Compound **3** decomposes within the temperature range of 380–410 °C, while all other compounds decomposed at lower temperatures. Compounds **4**, **5**, and **6** decompose within the temperature ranges 230–340, 250–300, and 250–320 °C, respectively.

Photoluminescence Study. The modification of photoluminescent properties of any organic molecule through co-crystallization or salt formation is an excellent approach. We have studied the photoluminescent properties of TBTA (**1**) and the compounds **2–6** in the solid state at room temperature. The excitation wavelength for all the compounds is 300 nm, and the maximum of the emission spectra is observed at 418 nm for **1**. The emission peaks were observed at 419 nm for hydrated TBTA (**2**), 420 nm for salt **3**, 420 nm for salt **4**, 425 nm for co-crystal **5**, and 416 nm for co-crystal **6**, shown in Figure 14. These peaks could be attributed to the π – π^* /n– π^* transitions occurring in TBTA. The nature of the luminescence spectra of the hydrate, salts, and co-crystals of TBTA are similar to that of TBTA, but the intensity of the emission peaks gradually decreases from **1** to **5**. It is noteworthy that the luminous intensity of the salts and co-crystals drastically depends on the change in polarity of the environment around TBTA. Therefore, the environmental polarity, as well as the formation of hydrogen bonds, has been suggested as the possible reason for the light switch effect for the salts of TBTA. On the other hand, for co-crystals, luminescent intensity might be decreased because effective transfer of charge via excited states of co-crystals does not take place due to inbuilt strain in the lattice. The shoulder peaks in the short-wave edge of the compounds **1–6** have been observed around 385 nm.

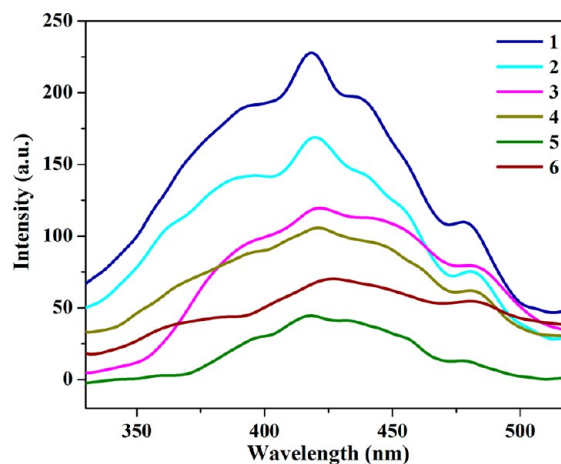


Figure 14. Photoluminescence spectra of all compounds.

The short-wave edges of the luminescence spectra are steeper than long-wave edges. The short-wave edges are observed due to purely electronic transition, and the other peaks in the luminescence spectra are observed due to different types of hydrogen bonding and π ··· interactions.

Schottky Barrier Effect of Compound 3. We have studied the UV–vis spectra of salt **3** in the solid state and determined the optical band gap (Figure S15, Supporting Information). The optical band gap is 2.92 eV, so it is expected that **3** can potentially behave as a semiconductor. Now to observe the electrical transport properties of **3**, we have fabricated an ITO/**3**/Al sandwich structure and performed the current–voltage (*I*–*V*) measurement, Figure 15. The forward current of the device shows

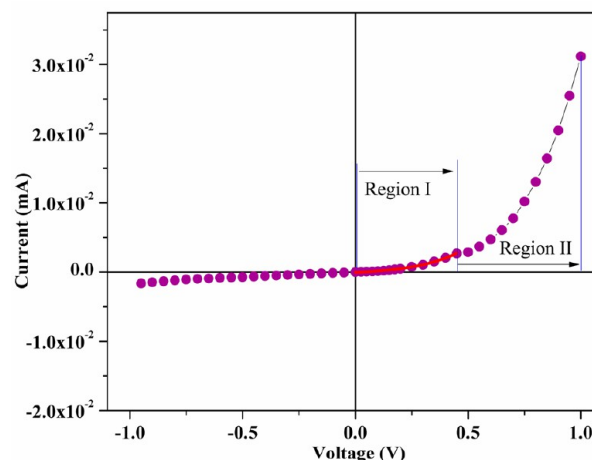


Figure 15. *I*–*V* characteristics of ITO/**3**/Al sandwich structure (regions I and II indicate the thermionic and space charge limited current regions, respectively).

a nonlinear behavior, while the reverse current increases slowly with bias voltage; the device acts like a diode. It is well-known that metal–semiconductor contact can exhibit rectifying character due to the Schottky barrier effect.³⁷ The on/off current ratio (i.e., rectification ratio) of the device is 19.1 at ± 1 V, which is appreciably high. The charge transport mechanism of the device can be realized by $\ln(I)$ vs *V* and $\ln(I)$ vs $\ln(V)$ plots (Figure S15, Supporting Information). According to $\ln(I)$ vs *V* and *I* vs *V* plots, the device displays exponential behavior in region I (Figure 15, in the voltage range 0 to +0.45 V), which can

be attributed to thermionic emission, and the $\ln(I)$ vs $\ln(V)$ plot (in the voltage range 0.5 to 1.0 V) obeys power law behavior ($I \propto V^n$; here $n = 3.5$); where the transport mechanism is governed by space charge limited current (SCLC) and recombination rate.

As per the $\ln(I)$ vs V plot (Figure S16, Supporting Information), in the low voltage region, the ideality factor (η) is ~ 2.97 . Because the I – V characteristics in the lower voltage region exhibit exponential behavior, we have determined the ideality factor (η), Schottky barrier height (Φ_b), and series resistance (R_s) following the formalism proposed by S. K. Cheung and N. W. Cheung.^{37b} According to them, the ideality factor and the effective series resistance of a Schottky contact can be calculated from the intercept and the slope, respectively, of the $dV/d[\ln(I)]$ vs I curve (Figure S17). The values of ideality factor and series resistance of the device are 2.96 and 48 k Ω , respectively. Now to evaluate the Schottky barrier height (Φ_b), we can define a function $H(I)$ as $H(I) = R_s I + \eta \Phi_b$. The $H(I)$ vs I curve will be a straight line with intercept $\eta \Phi_b$, and using the value of η (2.96), Φ_b can be determined. The Schottky barrier height of the present device is 0.66 eV. The value of the series resistance R_s determined from the slope of the $H(I)$ vs I plot is 58 k Ω . Thus, the values of R_s and η obtained by different formalisms match with each other, and the value of Φ_b corroborates with the earlier result obtained for an organic Schottky barrier diode.¹⁴ This proves the consistency of our analysis on Schottky behavior of the device. It may be noted that the ideality factor for the Schottky diode is unity. In the present case, the ideality factor is larger than unity, which can be ascribed to a high probability of electron–hole recombination in the depletion region and inhomogeneity of barrier height.³⁸ In conclusion, the results of I – V measurement clearly reveal that the ITO/3/Al sandwich structure behaves as a “Schottky barrier diode”.

Results of electrical transport property measurements clearly reveal that 3 is an organic semiconductor. It may be noted that there is a high demand for organic semiconductors for the fabrication of electronic devices like field effect transistors (FETs), light emitting diodes (LEDs), photovoltaic cells, and Schottky barrier diodes because of their low cost and environmentally friendly characters.^{39–41} Although organic semiconductors are considered as substitutes of silicon, until now there are only few examples of such class of compounds. Recently, the charge assisted hydrogen bonded and extended π -conjugated organic compounds have emerged as promising semiconductors. In the present case, salt 3 exhibits semiconducting behavior due to the presence of strong charge assisted $N1^+ \cdots H1 \cdots O1^-$ hydrogen bonding interactions between $bipy^{2+}$ and $TBTA^{2-}$ ions leading to the formation of supramolecular 1D chain.

CONCLUSIONS

We have successfully established the efficiency of TBTA to design multicomponent co-crystals and salts and studied their relevant functional properties. While chlorinated, fluorinated, and iodinated organic molecules are widely used in co-crystallization, in contrast appropriate attention has not been paid to brominated organic molecules, and thus TBTA is an excellent choice in this respect. Supramolecular structure analysis of TBTA reveals that the $O-H \cdots Br$ interactions connect the TBTA moieties to form a 2D supramolecular sheet structure rather than the formation of $-(COOH)_2$ synthon through supramolecular $O-H \cdots O$ hydrogen bonding interactions. The Br atom also participates in $\pi \cdots$ interactions to build the self-assembled supramolecular network. In addition, TBTA can

participate in supramolecular hydrogen bonding and $\pi \cdots$ interactions using carboxylate groups and $\pi \cdots$ rings. So, with the assistance of these supramolecular interactions, TBTA can potentially form multicomponent co-crystals and salts.

Based on the number of acceptor sites in organic base molecules, bicarboxylic TBTA forms co-crystals or salts in 1:1 and 1:2 ratios. Base molecules having single acceptor site form co-crystals or salts in 1:2 acid–base ratio, while base molecules having two acceptor sites form co-crystals or salts in 1:1 ratio, and this consequently dictates the formation of supramolecular trimer or supramolecular 1D chain through $O-H \cdots N/O^- \cdots H-N^+$ hydrogen bonding interactions between the acid–base pair. We have further attempted to reveal the cause behind the participation of water in crystallization and also the significance of it in overall supramolecular structures of the compounds. Hirshfeld surface analyses and the corresponding fingerprint plots reveal the intermolecular interactions in which TBTA participates with itself, with other organic molecules, and also with solvent water molecules in the crystal structures.

The photoluminescence study of the compounds reveals that with change of polarity around the TBTA molecules luminescent intensity has been modified. The electrical transport property measurements suggest that salt 3 is an organic semiconductor which can be attributed to the formation of supramolecular 1D chain through charge assisted hydrogen bonds between the acid and base molecules. The ITO/3/Al sandwich structure exhibits Schottky diode behavior with excellent rectification ratio. The ideality factor and barrier height of the device are 2.96 and 0.66 eV, respectively. Because of the diversity and versatility of the co-crystallization approach, we are now involved in designing and synthesizing novel functional materials by tuning both the physical and chemical properties of any organic molecule through co-crystallization.

ASSOCIATED CONTENT

Supporting Information

Figures and tables for supramolecular interactions. This material is available free of charge via the Internet at <http://pubs.acs.org>. CCDC 946553, 946564, 946554, 946555, 946565, and 900692 contain the supplementary crystallographic data for 1, 2, 3, 4, 5, and 6, respectively. These data can be obtained free of charge via <http://www.ccdc.cam.ac.uk/conts/retrieving.html>.

AUTHOR INFORMATION

Corresponding Authors

*E-mail: kumars@phys.jdvu.ac.in (S.K.).

*E-mail: rajatinorg1@gmail.com (R.S.).

Notes

The authors declare no competing financial interest.

ACKNOWLEDGMENTS

R.S. acknowledges financial support from the Council of Scientific and Industrial Research (CSIR), New Delhi, under the SRF program (09/096(0565)2008-EMR-I). Financial support from the University Grants Commission, New Delhi, and the Department of Science and Technology, Government of India, through DRS (SAP-I) and FIST programs to Department of Physics, Jadavpur University, for purchasing the X-ray powder diffractometer is gratefully acknowledged. We thank Mr. Debajyoti De, Department of Physics, NITMAS, for his helpful discussions.

DEDICATION

This article is dedicated to the memory of our beloved colleague the Late Dr. Golam Mostafa (1962–2011).

REFERENCES

- (1) (a) Desiraju, G. R. *Crystal Engineering: The Design of Organic Solids*; Elsevier: Amsterdam, 1989. (b) Nangia, A. J. *Chem. Sci.* **2010**, *1*, 295–310. (c) Moulton, B.; Zaworotko, M. J. *Chem. Rev.* **2001**, *101*, 1629–1658. (d) Zaworotko, M. J. *Cryst. Growth Des.* **2007**, *7*, 4–9. (e) Aakeröy, C. B.; Beatty, A. M.; Tremayne, M. D.; Rowe, M.; Seaton, C. C. *Cryst. Growth Des.* **2001**, *1*, 377–382.
- (2) (a) Desiraju, G. R. *Angew. Chem., Int. Ed.* **1995**, *34*, 2311–2327. (b) Steed, J. W.; Atwood, J. L. *Supramolecular Chemistry*; John Wiley & Sons, Ltd.: Chichester, U.K., 2000. (c) Desiraju, G. R.; Steiner, T. *The Weak Hydrogen Bond in Structural Chemistry and Biology*; Oxford University Press: Oxford, U.K., 1999. (d) Jeffrey, G. A.; Saenger, W. *Hydrogen Bonding in Biological Structures*; Springer: Berlin, 1991. (e) Hamilton, W. C.; Ibers, J. A. *Hydrogen Bonding in Solids*; Benjamin: New York, 1968. (f) Scheiner, S. *Hydrogen Bonding: A Theoretical Perspective*; Oxford University Press: Oxford, U.K., 1997. (g) Jeffrey, G. A. *An Introduction to Hydrogen Bonding*; Oxford University Press: Oxford, U.K., 1997. (h) Steiner, T. *Angew. Chem., Int. Ed.* **2002**, *41*, 48–76. (i) Zhang, Y.; Yang, Z.; Yuan, F.; Gu, H.; Gao, P.; Xu, B. *J. Am. Chem. Soc.* **2004**, *126*, 15028–15029. (j) Noro, S. I.; Akutagawa, T.; Nakamura, T. *Cryst. Growth Des.* **2007**, *7*, 1205–1208.
- (3) (a) Lehn, J. M. *Supramolecular Chemistry: Concepts and Perspectives*; VCH: Weinheim, Germany, 1995. (b) Lehn, J. M. *Rep. Prog. Phys.* **2004**, *67*, 249–265.
- (4) (a) Tanise, R.; Kapildev, S.; Arora, K.; Vishweshwar, P.; Zaworotko, M. J. *Cryst. Growth Des.* **2008**, *8*, 4533–4545. (b) Broker, G. A.; Tiekink, E. R. T. *CrystEngComm* **2007**, *9*, 1096–1109. (c) Du, M.; Zhang, Z.; Wang, X.; Wu, H.; Wang, Q. *Cryst. Growth Des.* **2006**, *6* (8), 1867–1875 and references therein..
- (5) (a) Beko, S. L.; Schmidt, M. U.; Bond, A. D. *CrystEngComm* **2012**, *14*, 1967–1971. and references therein. (b) Desiraju, G. R.; Tothadi, S. *Cryst. Growth Des.* **2012**, *12*, 6188–6198. (c) Goswami, P. K.; Thaimattam, R.; Ramanan, A. *Cryst. Growth Des.* **2013**, *13*, 360–366.
- (6) (a) MacDonald, J. C.; Dorrestein, P. C.; Pilley, M. M. *Cryst. Growth Des.* **2001**, *1*, 29–38. (b) Aakeröy, C. B.; Fasulo, M. E.; Desper, J. *Mol. Pharmaceutics* **2007**, *4* (3), 317–322. (c) Lie, S.; Maris, T.; Malveau, C.; Beaudoin, D.; Helzy, F.; Wuesf, J. D. *Cryst. Growth Des.* **2013**, *13*, 1872–1877.
- (7) Allen, F. H.; Motherwell, W. D. S.; Raithby, P. R.; Shields, G. P.; Taylor, R. *New J. Chem.* **1999**, *23*, 25–34.
- (8) (a) Aakeroy, C. B.; Salmon, D. J. *CrystEngComm* **2005**, *72*, 439–448. (b) Bis, J. A.; Vishweshwar, P.; Weyna, D.; Zaworotko, M. J. *Mol. Pharmaceutics* **2007**, *4*, 401–416. (c) Bond, A. S. *CrystEngComm* **2007**, *9*, 833–834. (d) Dunitz, J. D. *CrystEngComm* **2003**, *5*, 506–506.
- (9) Mukherjee, A.; Desiraju, G. R. *Chem. Commun.* **2011**, *47*, 4090–4092.
- (10) (a) Roy, S.; Mondal, S. P.; Ray, S. K.; Biradha, K. *Angew. Chem.* **2012**, *124*, 1–5. (b) Yan, Y.; Chen, J.-M.; Geng, N.; Lu, T.-B. *Cryst. Growth Des.* **2012**, *12*, 2226–2233. (c) Tao, Q.; Chen, J. M.; Ma, L.; Lu, T.-B. *Cryst. Growth Des.* **2012**, *12*, 3144–3152. (d) Chadha, R.; Saini, A.; Jain, D. S.; Venugopalan, P. *Cryst. Growth Des.* **2012**, *12*, 4211–4224. (e) Sanphui, P.; Goud, N. R.; Khandavilli, U. B. R.; Nangia, A. *Cryst. Growth Des.* **2011**, *11*, 4135–4145. (f) Kapadia, P. P.; Ditzler, L. R.; Baltrusaitis, J.; Swenson, D. C.; Tivanski, A. V.; Pigge, F. C. *J. Am. Chem. Soc.* **2011**, *133*, 8490–8493.
- (11) Yan, D.; Delori, A.; Lloyd, G. O.; Friščić, T.; Day, G. M.; Jones, W.; Lu, J.; Wei, M.; Evans, D. G.; Duan, X. *Angew. Chem., Int. Ed.* **2011**, *50*, 12483–12486.
- (12) Aakeroy, C. B.; Forbes, S.; Desper, J. *J. Am. Chem. Soc.* **2009**, *131* (147), 17048–17049.
- (13) Kapadia, P. P.; Ditzler, L. R.; Baltrusaitis, J.; Swenson, D. C.; Tivanski, A. V.; Pigge, F. C. *J. Am. Chem. Soc.* **2011**, *133*, 8490–8493.
- (14) Singh, A. K.; Prakash, R. *RSC Adv.* **2012**, *2*, 5277–5283.
- (15) Dalapati, S.; Saha, R.; Jana, S.; Patra, A. K.; Bhaumik, A.; Kumar, S.; Guchhait, N. *Angew. Chem., Int. Ed.* **2012**, *51*, 12534–12537.
- (16) Werner, P. E.; Eriksson, L.; Westdahl, M. J. *J. Appl. Crystallogr.* **1985**, *18*, 367–370.
- (17) Rodriguez-Carvajal, J. In *Abstracts of the Satellite Meeting on Powder Diffraction of the XV Congress of the IUCr, Toulouse, France*; IUCr: Chester, U.K., 1990; p 127.
- (18) Altomare, A.; Camalli, M.; Cucci, C.; Giacovazzo, C.; Moliterni, A.; Rizzi, R. *J. Appl. Crystallogr.* **2009**, *42*, 1197–1202.
- (19) Favre-Nicolin, V.; Cerny, R. *J. Appl. Crystallogr.* **2002**, *35*, 734–743. <http://objcryst.sourceforge.net>.
- (20) Stewart, J. J. *J. Mol. Model.* **2007**, *13*, 1173–1213.
- (21) Larson, A. C.; Von Dreele, R. B. *General Structure Analysis System (GSAS)*, Los Alamos National Laboratory Report LAUR, Los Alamos, NM, 2000, p 86.
- (22) Toby, B. H. *J. Appl. Crystallogr.* **2001**, *34*, 210–213.
- (23) Sheldrick, G. M. *SHELXS 97, Program for Structure Solution*; University of Göttingen: Germany, 1997.
- (24) Sheldrick, G. M. *SHELXL 97, Program for Crystal Structure Refinement*; University of Göttingen: Germany, 1997.
- (25) Spek, A. L. *PLATON, Molecular Geometry Program. J. Appl. Crystallogr.* **2003**, *36*, 7–13.
- (26) Farrugia, L. J. *J. Appl. Crystallogr.* **1997**, *30*, 565–566.
- (27) Farrugia, L. J. *J. Appl. Crystallogr.* **1999**, *32*, 837–838.
- (28) (a) Spackman, M. A.; Jayatilaka, D. *CrystEngComm* **2009**, *11*, 249–253. (b) Hirshfeld, F. L. *Theor. Chim. Acta* **1977**, *44*, 129–138. (c) Clausen, H. F.; Chevallier, M. S.; Spackman, M. A.; Iversen, B. B. *New J. Chem.* **2010**, *34*, 193–199.
- (29) (a) Spackman, M. A.; Byrom, P. G. *Chem. Phys. Lett.* **1997**, *267*, 215–220. (b) McKinnon, J. J.; Mitchell, A. S. *Chem.—Eur. J.* **1998**, *4*, 2136–2141.
- (30) (a) Rohl, L.; Moret, M.; Kaminsky, W.; Claborn, K.; McKinnon, J. J.; Kahr, B. *Cryst. Growth Des.* **2008**, *8*, 4517–4525. (b) Parkin, A.; Barr, G.; Dong, W.; Gilmore, C. J.; Jayatilaka, D.; McKinnon, J. J.; Spackman, M. A.; Wilson, C. C. *CrystEngComm* **2007**, *9*, 648–652. (c) Spackman, M. A.; McKinnon, J. J. *CrystEngComm* **2002**, *4*, 378–392.
- (31) Wolff, S. K.; Grimwood, D. J.; McKinnon, J. J.; Jayatilaka, D.; Spackman, M. A. *Crystal Explorer 2.0*; University of Western Australia: Perth, Australia, 2007.
- (32) Frisch, M. J.; Trucks, G. W.; Schlegel, H. B.; Scuseria, G. E.; Robb, M. A.; Cheeseman, J. R.; Scalmani, G.; Barone, V.; Mennucci, B.; Petersson, G. A.; Nakatsuji, H.; Caricato, M.; Li, X.; Hratchian, H. P.; Izmaylov, A. F.; Bloino, J.; Zheng, G.; Sonnenberg, J. L.; Hada, M.; Ehara, M.; Toyota, K.; Fukuda, R.; Hasegawa, J.; Ishida, M.; Nakajima, T.; Honda, Y.; Kitao, O.; Nakai, H.; Vreven, T.; Montgomery, J. A., Jr.; Peralta, J. E.; Ogliaro, F.; Bearpark, M.; Heyd, J. J.; Brothers, E.; Kudin, K. N.; Staroverov, V. N.; Kobayashi, R.; Normand, J.; Raghavachari, K.; Rendell, A.; Burant, J. C.; Iyengar, S. S.; Tomasi, J.; Cossi, M.; Rega, N.; Millam, J. M.; Klene, M.; Knox, J. E.; Cross, J. B.; Bakken, V.; Adamo, C.; Jaramillo, J.; Gomperts, R.; Stratmann, R. E.; Yazyev, O.; Austin, A. J.; Cammi, R.; Pomelli, C.; Ochterski, J. W.; Martin, R. L.; Morokuma, K.; Zakrzewski, V. G.; Voith, G. A.; Salvador, P.; Dannenberg, J. J.; Dapprich, S.; Daniels, A. D.; Farkas, O.; Foresman, J. B.; Ortiz, J. V.; Cioslowski, J.; Fox, D. J. *Gaussian 09*, revision E.01; Gaussian, Inc.: Wallingford, CT, 2009.
- (33) Kumagai, H.; Kawata, S. *Acta Crystallogr.* **2011**, *E67*, o2636.
- (34) (a) Etter, M. C.; MacDonald, J. C.; Bernstein, J. *Acta Crystallogr.* **1990**, *B46*, 256–262. (b) Etter, M. C. *Acc. Chem. Res.* **1990**, *23*, 120–126.
- (35) (a) Aakeröy, C. B.; Fasulo, M. E.; Desper, J. *Mol. Pharmaceutics* **2007**, *4*, 317 and references therein. (b) Stilić, V.; Kaitner, B. *Cryst. Growth Des.* **2012**, *12*, 5763–5772.
- (36) (a) Clarke, H. D.; Arora, K. K.; Bass, H.; Kavuru, P.; Ong, T. T.; Pujari, T.; Wojtas, L.; Zaworotko, M. J. *Cryst. Growth Des.* **2010**, *10*, 2152–2167. (b) Aakeroy, C. B.; Forbes, S.; Desper, J. *CrystEngComm* **2012**, *14*, 2435–2443.
- (37) (a) Streetman, B. G. *Solid state electronic devices*, 4th ed.; Prentice hall of India: New Delhi, 2000. (b) Cheung, S. K.; Cheung, N. W. *Appl. Phys. Lett.* **1986**, *49* (2), 85–87.

- (38) Campos, M.; Bulhoes, L. O. S.; Lindino, C. A. *Sens. Actuators A* **2000**, *87*, 67–71.
- (39) (a) Yu, A.-D.; Kurosawa, T.; Lai, Y.-C.; Higashihara, T.; Ueda, M.; Liu, C.-L.; Chen, W.-C. *J. Mater. Chem.* **2012**, *22*, 20754–20763. (b) Chen, L.; Wang, L.; Gao, X.; Nagase, S.; Honsho, Y.; Saeki, A.; Seki, S.; Jiang, D. *Chem. Commun.* **2009**, 3119–3121. (c) Huang, M.; Schilde, U.; Kumke, M.; Antonietti, M.; Cölfen, H. *J. Am. Chem. Soc.* **2010**, *132*, 3700–3707. (d) Zheng, Q.; Huang, J.; Sarjeant, A.; Katz, H. E. *J. Am. Chem. Soc.* **2008**, *130*, 14410–14411.
- (40) (a) Niimi, K.; Mori, H.; Miyazaki, E.; Osaka, I.; Kakizoe, H.; Takimiya, K.; Adachi, C. *Chem. Commun.* **2012**, *48*, 5892–5894. (b) Chen, S.-C.; Zhang, Q.; Zheng, Q.; Tang, C.; Lu, C.-Z. *Chem. Commun.* **2012**, *48*, 1254–1256.
- (41) Chabiniy, M. L.; Chen, X.; Holmlin, R. E.; Jacobs, H.; Skulason, H.; Frisbie, C. D.; Mujica, V.; Ratner, M. A.; Rampi, M. A.; Whitesides, G. M. *J. Am. Chem. Soc.* **2002**, *124*, 1173–11736.